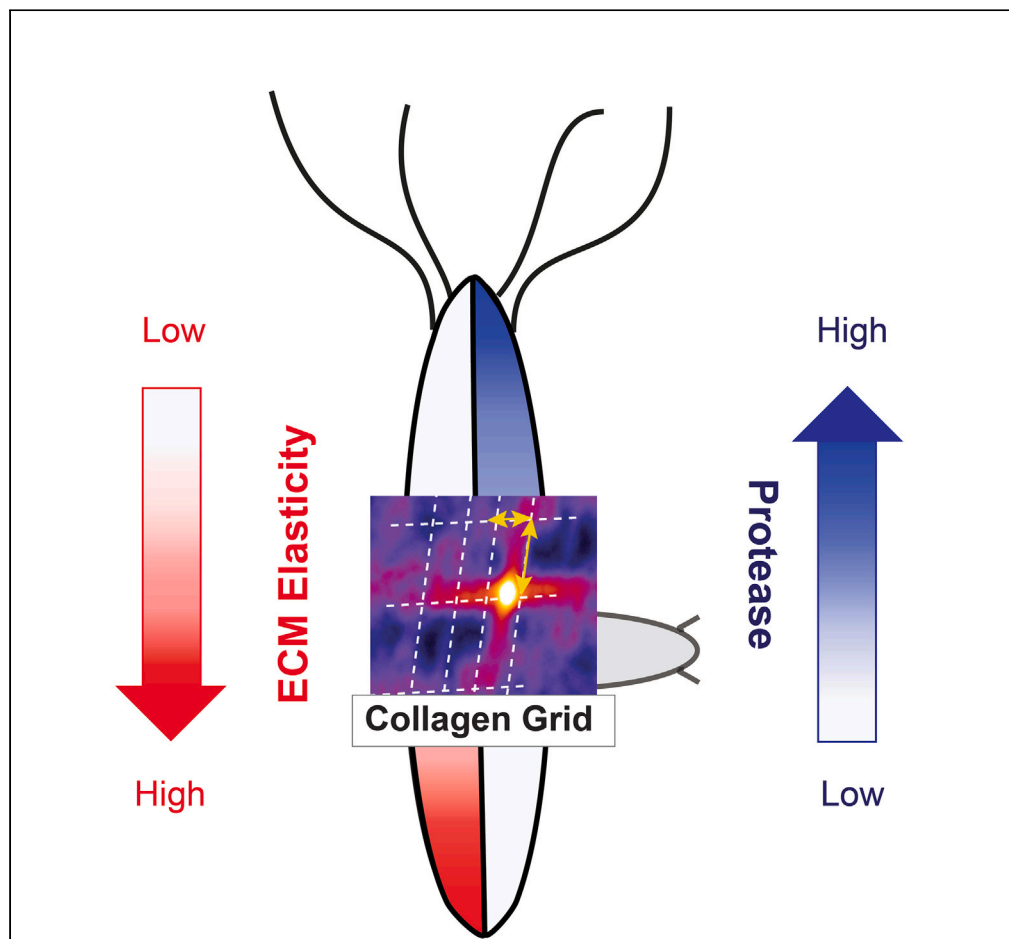**Article**

Wnt/β-catenin signaling induces axial elasticity patterns of *Hydra* extracellular matrix

Mariam Veschgini,
Ryo Suzuki, Svenja
Kling, ..., Suat
Özbek, Thomas
W. Holstein,
Motomu Tanaka

thomas.holstein@cos.
uni-heidelberg.de (T.W.H.)
tanaka@uni-heidelberg.de
(M.T.)

Highlights

Hierarchical structural order of *Hydra* ECM correlates with tissue morphogenesis

Elasticity patterns and structural order are tightly connected to tissue patterning

Gradients of matrix protease govern elasticity patterns of *Hydra* ECM

Wnt/β-catenin signaling acts on *Hydra* ECM structural order and elasticity

Article

Wnt/β-catenin signaling induces axial elasticity patterns of *Hydra* extracellular matrix

Mariam Veschgini,[1] Ryo Suzuki,[1,2] Svenja Kling,[3] Hendrik O. Petersen,[3] Bruno Gideon Bergheim,[3] Wasim Abuillan,[1] Philipp Linke,[1] Stefan Kaufmann,[1] Manfred Burghammer,[4] Ulrike Engel,[3,5] Frank Stein,[6] Suat Özbek,[3] Thomas W. Holstein,[2,3,*] and Motomu Tanaka[1,2,7,*]

SUMMARY

The extracellular matrix (ECM) plays crucial roles in animal development and diseases. Here, we report that Wnt/β-catenin signaling induces the ECM remodeling during *Hydra* axis formation. We determined the micro- and nanoscopic arrangement of fibrillar type I collagen along *Hydra's* body axis using high-resolution microscopy and X-ray scattering. Elasticity mapping of the ECM *ex vivo* revealed distinctive elasticity patterns along the body axis. A proteomic analysis of the ECM showed that these elasticity patterns correlate with a gradient-like distribution of metalloproteases along the body axis. Activation of the Wnt/β-catenin pathway in wild-type and transgenic animals alters these patterns toward low ECM elasticity patterns. This suggests a mechanism whereby high protease activity under control of Wnt/β-catenin signaling causes remodeling and softening of the ECM. This Wnt-dependent spatiotemporal coordination of biochemical and biomechanical cues in ECM formation was likely a central evolutionary innovation for animal tissue morphogenesis.

INTRODUCTION

The extracellular matrix (ECM) regulates the homeostasis of animal tissues, supporting the structural integrity and cell functions.[1] ECM remodeling plays vital roles in regulating not only behaviors of single cells[2] but also the morphogenesis of tissues, where it is accompanied by large-scale deformations, such as tissue invagination during gastrulation or the immigration and convergent extension of cells.[3–5] Many diseases are also characterized by the significant remodeling of ECM, such as the myelofibrosis in bone marrow causing pancytopenia[6] and stiffening of pulmonary ECM in fibrotic lung tissues.[7] However, despite accumulating knowledge on participating proteins and key signaling pathways, little is understood how ECM elasticity correlates with tissue morphogenesis.[3] Barriga et al. indented cut pieces of *Xenopous laevis'* mesoderm with atomic force microscopy (AFM) and demonstrated by using head mesoderm of different age as well as hydrogels that the collective migration of neural crest cells during morphogenesis requires a stiffening of mesoderm.[8,9] However, direct elasticity measurements of the ECM as a function of morphogenesis have not been reported so far. The use of a model animal with a simpler body design is therefore a straightforward strategy.

In this paper, we investigated the temporal progression of ECM elasticity during tissue growth in the freshwater polyp *Hydra*. *Hydra* is a member of the >600 million-years-old phylum Cnidaria and a paradigm for an almost unlimited growth and regeneration capability. Compared to bilaterian animals, it has a simple, sack-like body plan with a body wall composed of an ECM, called mesoglea, which separates two cell layers; an outer ectoderm; and an inner endoderm. Previous accounts showed that the mesoglea plays an important role in asexual reproduction of *Hydra* through budding. Mesoglea undergoes dynamic remodeling in order to support the daughter animal (bud) stemming out of the main body axis of a mother *Hydra*.[10–12] This body axis is an oral-aboral (OA) axis with an oral "head" and an aboral "foot". It is equivalent to the posterior-anterior axis of bilaterians (for details, see the review by Holstein[13]).

Intriguingly, the molecular composition of *Hydra* mesoglea is very similar to that of vertebrate ECM, containing heparan sulfate, laminin, and fibronectin-like molecules as well as fibrillar (type I and II) and non-fibrillar (type IV) collagens.[12,14–16] *Hydra* ECM combines two major ECM functions that are separated

in higher animals, i.e., mechanical integrity guaranteed by collagen fibers in connective tissues and epithelial tissue organization mediated by the basal lamina.[15] To accommodate both functions, *Hydra* mesoglea is supposed to form a tri-laminar structure: two thin sub-epithelial zones based on collagen type IV and laminin sandwich a central fibrous zone, the interstitial matrix consisting of a grid of collagen type I fibrils (HCol-I).[17–19] The dynamic morphological change during growth and patterning is supported by a remodeling of ECM collagen fibers.[20–22] Immunofluorescence labeling of HCol-I revealed that the mesoglea of an evaginating bud showed weaker signals compared to the mother polyp, which was attributed to the thinning of mesoglea in order to accommodate a large number of cells flowing out from the parental *Hydra*.[23] The thinning of the ECM naturally suggested that rapidly growing buds are softer, but there has been no quantitative study on how tissue morphogenesis of *Hydra* correlates with the local structural orders and elasticity of ECM during patterning and asexual reproduction.

To unravel how the asymmetric stretching along *Hydra*'s OA axis originates from the hierarchical arrangement of ECM proteins, we investigated the spatial ordering patterns of HCol-I in the mesoglea along *Hydra*'s body axis using high-resolution microscopy and autocorrelation analysis. To gain further insight into the nanometer-scale organization of the mesoglea, we performed grazing-incidence small-angle X-ray scattering with a nano-focused synchrotron beam (nano-GISAXS).[24,25]

To extract characteristic spatiotemporal patterns of ECM elasticity during budding and hence the break of the radial symmetry, we measured the local elasticity of *Hydra* mesoglea isolated at different time points along the body axis by atomic force microscopy (AFM) nano-indentation. Different from whole-animal explants,[9] where cut pieces of tissue are always a function of the ECM and the overlying cells, this approach allows direct characterization of the ECM elasticity. To demonstrate the influence of canonical Wnt signaling on the spatiotemporal change in ECM elasticity, we performed quantitative proteome analysis of transgenic *Hydra* overexpressing Wnt3 as well as wild-type *Hydra* treated with glycogen synthase kinase 3β (GSK3β) inhibitor (Alsterpaullone). As presented in the following sections, our data suggest that ECM remodeling is part of the Wnt-regulated patterning process during *Hydra* axis formation.

RESULTS

Micro- and nanoscopic arrangements of *Hydra* ECM

First, we performed immunofluorescence confocal microscopy imaging of whole *Hydra* ECM by staining isolated mesoglea with HCol-I (Figure 1) and laminin antibodies (Figure S1. Immunofluorescence images of *Hydra* ECM *ex vivo* after de-cellularization, related to Figure 1.). The direct comparison of images taken *in vivo* (Figure 1A) and *ex vivo* (Figure 1B) confirmed that the intact mesoglea was maintained after de-cellularization. Figures 1C, 1E, and 1G represent the confocal images collected from 50 × 50 μm^2 areas from different body regions, suggesting that the bundles of HCol-I take grid-like structures.[26] The characteristic pattern was extracted by an autocorrelation analysis of confocal images (Figures 1D, 1F, and 1H). As indicated by white broken lines, HCol-I near the hypostome shows a parallel arrangement with a characteristic spacing of 5 ± 1 μm (Figure 1D). Notably the direction of fiber assembly does not seem to correlate with the OA axis. On the other hand, HCol-I takes distorted rectangular arrangements in the middle region (Figure 1F) and the region close to the peduncle zone (Figure 1H). The characteristic unit length that slightly deviates from the OA axis ($\leq 10°$) was 10 ± 2 μm, while the other unit length taking the angle of 100 ± 10° was about one-half, 5 ± 1 μm. The data indicate that the HCol-I bundles aligned in the direction parallel to the OA axis are more tightly packed compared to the ones that are assembled almost perpendicular to the body axis. The anisotropic arrangement of HCol-I bundles observed in these regions seems reasonable because *Hydra* undergoes a significant axial stretching and contraction. Currently, we cannot explain whether the apparent deviation from an ideal rectangle arrangement reflects either original structural features, such as spiral arrangement, or a mechanical distortion caused by the chemical fixation.

It should be noted that the anisotropic structural patterns of *Hydra* ECM obtained above are of micrometer-scale and hence coincide with the arrangement of HCol-I bundles. To unravel the molecular-level arrangement of HCol-I parallel and perpendicular to the OA axis, we probed the nanoscale structures of *Hydra* ECM by using nano-GISAXS. Figure 2A schematically illustrates the experimental setup and sample geometry. The isolated *Hydra* mesoglea was deposited on a Si_3N_4 membrane. A monochromatic, focused synchrotron X-ray (beam diameter: 200 nm) impinges to the sample at an incident angle $\alpha_i = 0.46°$, which is beyond the critical angle of total external reflection ($\alpha_c = 0.14°$). Figures 2B and 2C represent nano-GISAXS patterns of the mesoglea obtained from directions parallel or perpendicular to the body axis, respectively.
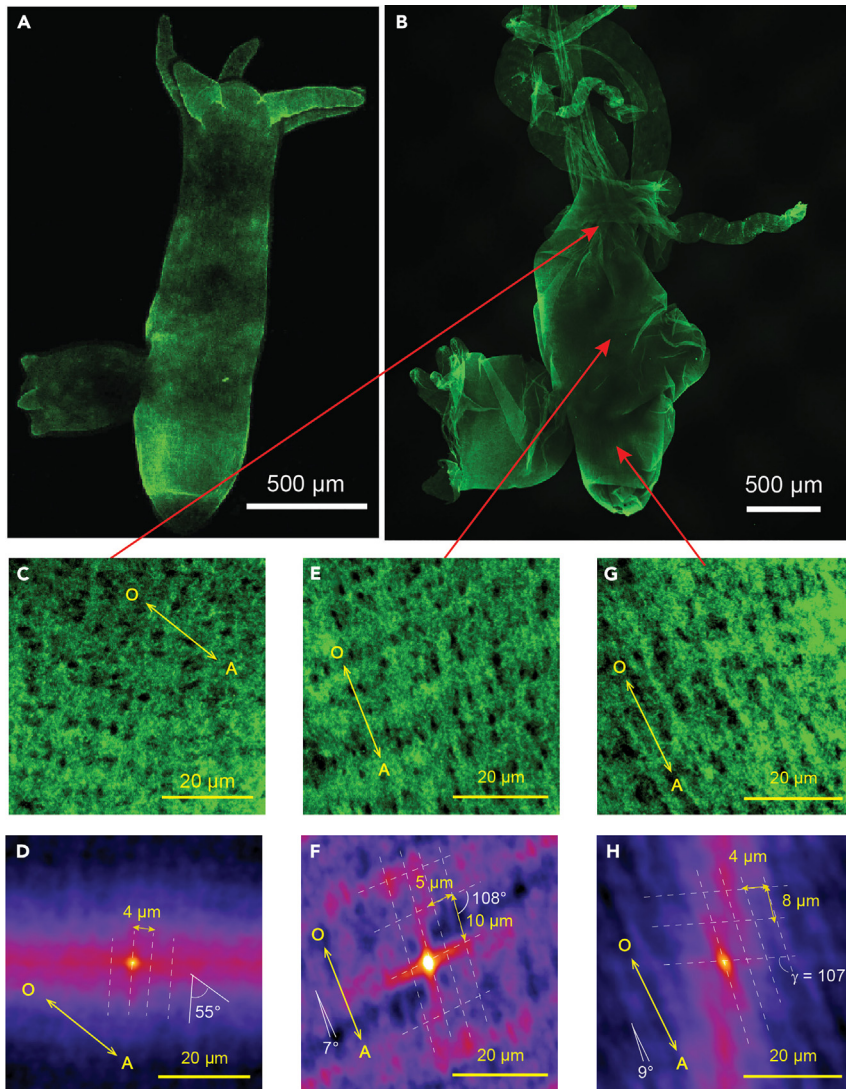
Figure 1. Micrometer-scale orders of *Hydra* ECM (mesoglea) by autocorrelation analysis of high-resolution microscopy images

(A and B) Confocal immunofluorescence image of a whole *Hydra* ECM stained with fibrillar type I collagen (Hcol-I) antibody *in vivo* (a) and *ex vivo* (b).

(C, E, and G) Confocal images collected from 50 × 50 μm² areas from the regions indicated by red arrows.

(D, F, and H) Autocorrelation maps calculated from the confocal images. OA axis in each image is indicated by a yellow arrow. The characteristic features extracted from the analysis, such as unit cell length and angles, are indicated in each panel.

Several scattering patterns showed that one or more arcs were arranged concentrically around the direct beam, accompanied by additional satellite peaks positioned on the arcs (Figure 2D). The white grid overlaid on each pattern represents the reconstructed reciprocal lattice. The obtained lattice patterns clearly indicate that rod-like objects are aligned parallel to the substrate surface. The real space lattice parameters (a, b, γ) calculated from the GISAXS patterns parallel and perpendicular to the *Hydra* body axis are presented in the top and middle panels of Figure 1E, respectively. The lattice parameters of the mesoglea parallel to the OA axis are $a_{||} = (17.6 \pm 3.6)$ nm, $b_{||} = (6.7 \pm 0.8)$ nm, and $\gamma_{||} = (97.1 \pm 2.4)°$, implying that the rods take a distorted hexagonal arrangement. The corresponding data show that the rod-like objects also take an ordered structure perpendicular to the body axis resulting in a distorted hexagonal lattice with slightly different units, $a_{\perp} = (11.8 \pm 0.5)$ nm, $b_{\perp} = (4.3 \pm 0.4)$ nm, and $\gamma_{\perp} = (100.3 \pm 9.3)°$.
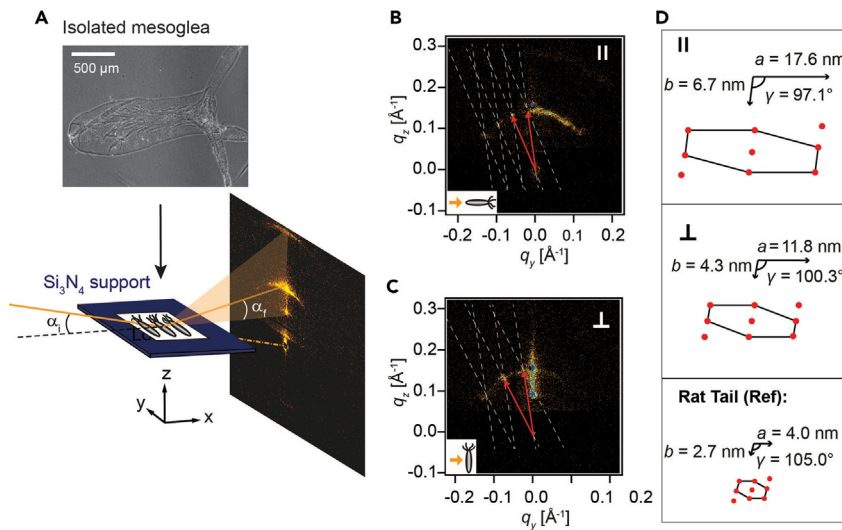
Figure 2. Nanometer-scale arrangement of HCol-I revealed by nano-GISAXS

(A–C) Top left: phase-contrast microscopy image of an isolated mesoglea. Bottom: experimental setup of nano-GISAXS. Isolated mesoglea was placed on a Si_3N_4 window and illuminated by a nano-focused X-ray beam (diameter: 200 nm) at a grazing incidence angle $\alpha_i = 0.46°$. Scattering patterns obtained from mesoglea, whose body axis was positioned parallel (b) or perpendicular (c) to the beam (see inset yellow arrow). The reciprocal lattice is indicated in white, and the lattice vectors in red.

(D) Lattice parameters in real space (a, b, γ) calculated from the directions parallel (top) and perpendicular (middle) to the major body axis. For comparison, the lattice parameters from the reference sample (collagen type I from rat tail tendon)[27] are presented (bottom).

We compared these lattice parameters with those of type I collagen from vertebrates (rat tail tendon) taken from a previous account ($a = 4.0$ nm, $b = 2.3$ nm, and $\gamma = 105.0°$,[27] bottom panel of Figure 2D). Similar opening angles ($\approx 100°$) suggest that the rod-like objects in *Hydra* mesoglea are fibrillar HCol-I.[17,18] Clearly different lattice parameters between the directions parallel and perpendicular to the OA axis indicate that the molecular-level arrangement of HCol-I is highly anisotropic. This seems to agree qualitatively well with the µm-scale arrangement of HCol-I bundles (Figure 1). Although the characteristic length scales extracted from confocal microscopy and nano-GISAXS differ approximately by three orders of magnitude, the anisotropically arranged HCol-I fibers and fiber bundles seem to support the large degree of extension and contraction of *Hydra* along the body axis. Moreover, the interfibrillar distances between HCol-I are about 2–4 times longer compared to those in rat tail tendon. This can be attributed to the lower proline content and lack of lysine crosslinks in HCol-I fibers.[18,28] Thus, our data on the hierarchical structural order of *Hydra* mesoglea indicate that HCol-I plays key roles in supporting the basal elasticity of *Hydra* mesoglea. This is also supported by our proteomic analysis, demonstrating that HCol-I is one of the highest abundant proteins in *Hydra* mesoglea (see below).

Elasticity mapping and classification of mechanical phenotypes

To monitor the change in mesoglea elasticity during asexual budding, we mapped the Young's modulus of *Hydra* mesoglea along the body axis by AFM nano-indentation.[29–31] Figure 3A shows a typical force-distance curve of *Hydra* mesoglea. Note that the readout from the instrument presented in Y axis is given in voltage, which is proportional to the force. We fitted the measured data (gray symbols) with the modified Hertz model[32] and calculated the Young's modulus. Prior to the analysis, we carefully optimized the tip-sample contact point z_0 as the calculated elastic modulus significantly depends on the accuracy of z_0.[33,34] As indicated by arrows in Figure 2A, the contact point candidate was marched over the points near the onset point to determine the optimal contact point (red). As presented in Figure 3B, we determined the elastic modulus E by minimizing the mean sum of square residuals (SSR). For each sample, 7–37 positions were indented. As shown in Figure 3C, the elasticity pattern was extracted by normalizing each indentation point with the relative position from the foot (i.e., the aboral terminus) ($d = 0$) to head with the mouth (i.e., the oral terminus) ($d = 1.0$) along the body axis. This enables us not only to compare different mesoglea samples but also to discern three key regions along the body axis: (i) the peduncle
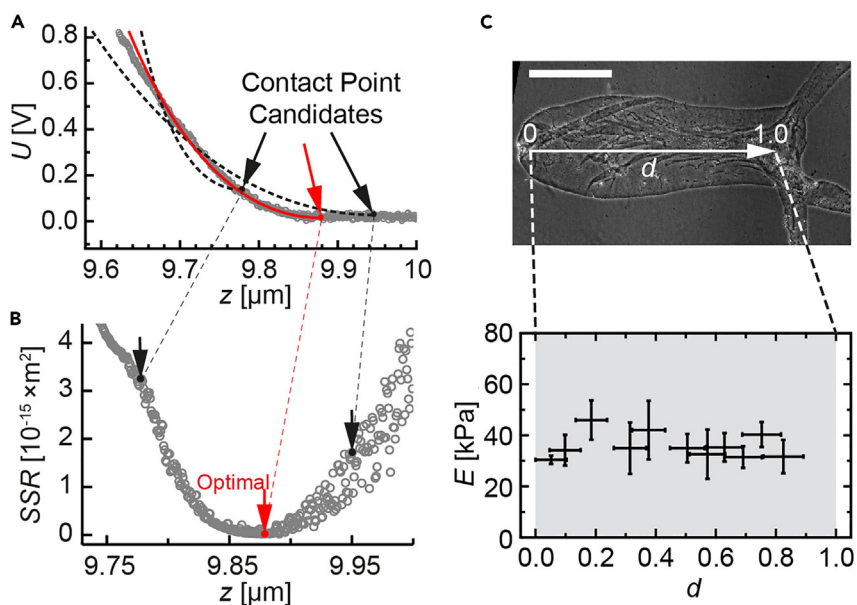
Figure 3. Elasticity mapping of *Hydra* mesoglea by AFM nano-indentation

(A) A typical force (voltage)-distance curve (gray circles) of a mesoglea isolated from a freshly detached *Hydra*. Three contact point candidates (indicated by arrows) and the corresponding fits are presented for comparison.

(B) The optimization of the fit by minimizing the mean sum of square residuals (SSR) during the marching of the contact point candidate. The optimal contact point (red) yields the bulk elastic modulus $E = 29.7$ kPa.

(C) Phase-contrast microscopy image of a mesoglea isolated from a freshly detached *Hydra*. The relative position from the foot ($d = 0$) to mouth ($d = 1.0$) along the body axis is used for the normalization of spatial information. Scale bar: 500 μm. "Elasticity map" of *Hydra* mesoglea along the body axis. Data are presented as means and standard deviations out of 8 independent measurements.

region at the aboral end ($0.0 \leq d < 0.1$), (ii) the budding region in the middle ($0.1 \leq d \leq 0.3$), and (iii) the upper gastric region at the oral end ($0.6 \leq d \leq 1.0$).

Utilizing the positional segmentation described above, the "elasticity maps" extracted from different polyps could be classified into three major elasticity patterns (Figure S2. Distribution of Young's moduli determined by AFM nano-indentation, related to Figure 4): ***Type A*** (Figure 4A) is characterized by uniform elastic moduli along the entire body column with $E \approx 40$ kPa. ***Type B*** (Figure 4B) exhibits distinctly higher elastic moduli in the peduncle and budding regions ($E \approx 120$ kPa) compared to the head region ($E \approx 20$ kPa). ***Type C*** (Figure 4C) looks similar to type B but shows lower elastic moduli in the peduncle region ($E \approx 50$ kPa). The overlay of the three main elasticity patterns is presented in Figure 4D. 97% of the measured elasticity patterns in mesoglea isolated from *Hydra* polyps (n = 38) at different time points could be classified into type A (66%), type B (18%), and type C (13%). Only one sample exhibited a random pattern, which could be attributed to artifacts from remaining nematocysts.[35]

Modulation of elasticity patterns

To unravel whether the extracted elasticity patterns correlate with the age or developmental stage of *Hydra*, we compared the elasticity patterns of freshly detached polyps ($t = 0$ days) and polyps at the ages of $t = 2$–3 days. The time window of 3 days was chosen in order to focus on the transition from newly detached buds to budding polyps. Mesoglea from freshly detached *polyps* ($t = 0$ days) showed exclusively type A pattern, i.e., the elasticity of mesoglea was low and uniform along the body axis. At $t = 2$ days, the mesoglea started taking type B and type C patterns ($\approx 60\%$), indicating an increase in the Young's modulus in the budding region. At $t = 3$ days, type B and type C were predominant ($\approx 80\%$). Although it is difficult to identify the very early stage of bud formation, the emergence of type B and type C can be attributed to the formation of buds. In fact, $t = 2$–3 days is the typical time window for freshly detached *Hydra* polyps to start budding.[36] ECMs of fast-growing buds became thinner with time,[23] resulting in a homogeneous and low-elasticity pattern (type A). Our data indicate that the growth process and maturation of freshly detached buds toward mature, bud-forming polyps are accompanied by the modulation of elasticity patterns in
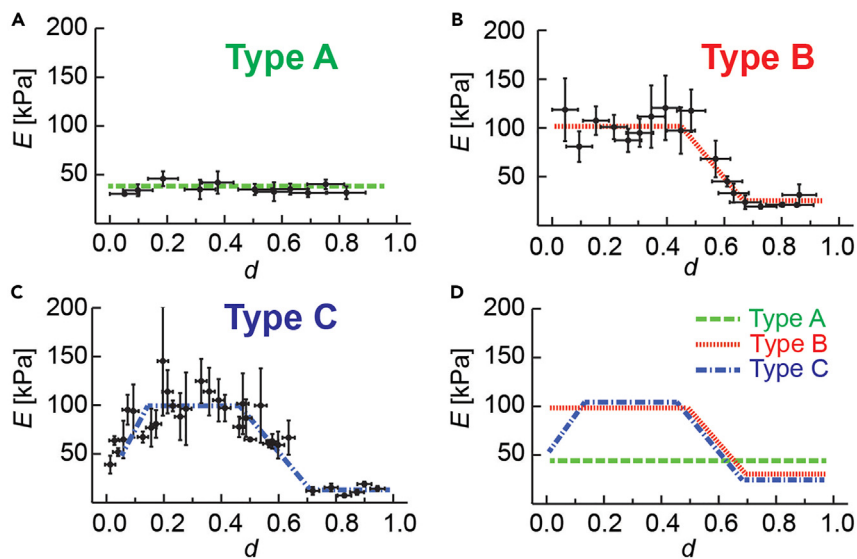
Figure 4. Three representative elasticity phenotypes of *Hydra* mesoglea (n = 38)

(A) Type A is characterized by a uniform, soft mesoglea.

(B) Type B shows higher elastic moduli in peduncle and budding regions compared to the head region.

(C) Type C looks similar to type B, but the elasticity in the peduncle region is distinctly lower. Data are presented as means and standard deviations.

(D) Overlay of three representative elasticity patterns.

Hydra ECM. It seems plausible that the growth of buds from mature *Hydra* polyps is supported by the new synthesis of ECM in the budding region, which is characterized by the conversion from type A to type B/C. Finally, the low elasticity levels in type C at the aboral end likely correlate with the maturation of polyps undergoing dynamic remodeling of the peduncle region.[37]

The molecular processes that enable the large-scale deformation must include either post-transcriptional modifications of ECM proteins or changes in expression and composition of ECM proteins (see below).

Elasticity patterns correlate with Wnt/β-catenin signaling

Budding and pattern formation in *Hydra* are strongly dependent on Wnt signaling.[38] Wnt Inhibitors like Dkk-1/2/4 and the Wnt-specific astacin protease HAS-7 are expressed in a gradient-like pattern along the OA axis of *Hydra* and act as antagonists against Wnt ligands.[39,40] We therefore analyzed to what extent the perturbation of the Wnt/β-catenin pathway can modulate the elasticity patterns of *Hydra* mesoglea. Polyps were treated with Alsterpaullone (Alp),[41] an inhibitor of GSK3β that induces the stable activation of β-catenin in a position-independent manner.[26,42] The treatment of polyps with 5 μM Alp leads to the formation of ectopic tentacles along the body column after 2–3 d[41] Figure 5A shows an optical microscopy image of an Alp-treated polyp (see STAR Methods). Compared to untreated controls, the mesoglea of Alp-treated polyps exhibited a dramatic decrease in its Young's moduli along the entire body column to $E \approx 35$ kPa (Figure 5B). The uniform distribution of lower E values suggests that the ordering of HCol-I is poorer. As shown in Figures 5C and 5D, the confocal immunofluorescence of HCol-I and the corresponding auto-correlation maps of Alp-treated *Hydra* ECM in the middle region show weak, fragmented patterns only in the direction parallel to the OA axis.

We also measured the elasticity patterns in mesoglea samples isolated from *Hydra vulgaris* overexpressing *Wnt3* (*HyActP::HyWnt3*) or β-catenin (*Hyβ-catenin::β-catenin-GFP*)[43–45] (Figure S3. Effect of Wnt/β-catenin signaling on phenotypes and elasticity patterns, related to Figure 5). In the β-catenin transgenic line, the phenotype is similar to polyps treated constantly with low-dose Alp showing ectopic tentacles and head structures,[38,44] while *Wnt3*-overexpressing polyps form well-defined ectopic body axis. Polyps from both transgenic lines exhibited uniform, low Young's moduli along the body axis (although the β-catenin transgenes were more diverging due to a broader diversity of morphological phenotypes).
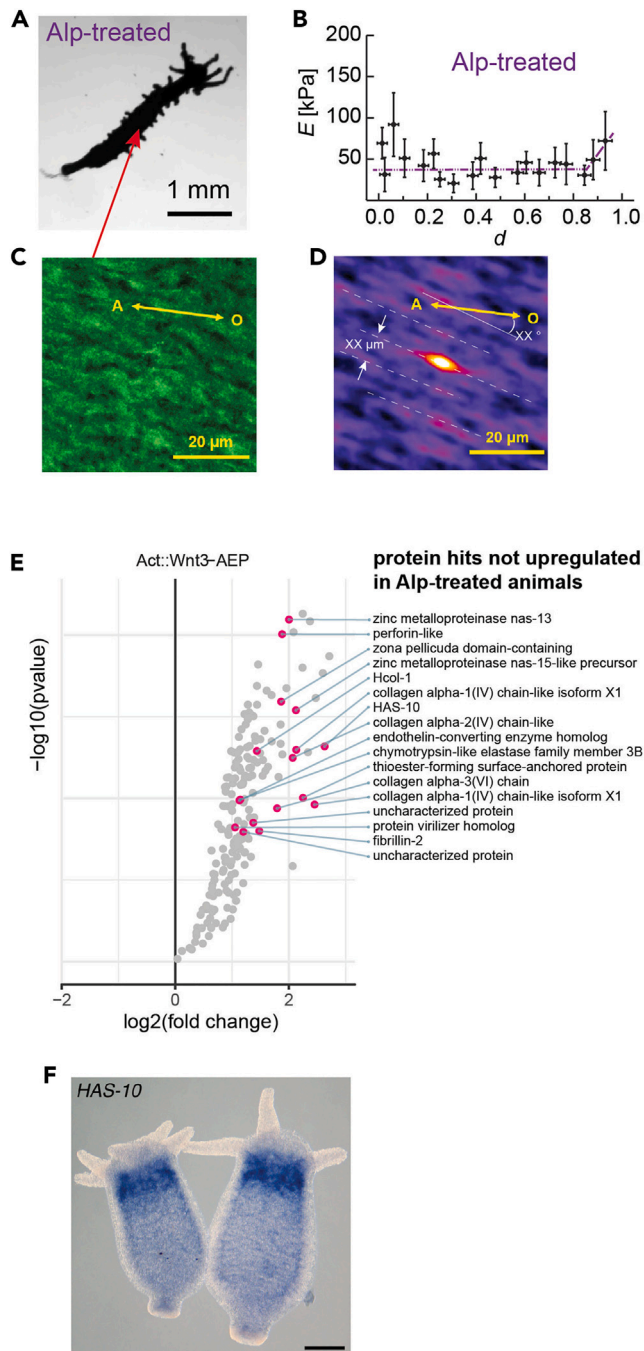
Figure 5. Effect of Wnt/β-catenin activation on elasticity pattern and protein-expression pattern

(A) Light-microscopy image of a polyp continuously treated with GSK3β inhibitor, Alsterpaullone (Alp), at t = 3 days.

(B) Elasticity pattern of mesoglea isolated from Alp-treated *Hydra*. Data are presented as means and standard deviations. The elastic moduli were low over the entire body column, which is clearly different from intact mesoglea (Figure 3). Immunofluorescence image.

(C) and the corresponding autocorrelation map.

(D) of *Hydra* Hcol-I after Alp treatment exhibiting a much weaker order compared to the control (Figure 1E).

(E) Volcano plot of proteins upregulated in transgenic HyActP:Wnt3 polyps compared to wild-type AEP. The annotations show a significant enrichment of proteases and fibrillar mesoglea components including Hcol-I in the transgenic line that

Figure 5. *Continued*

undergoes constant axis formation. The red dots denote enriched protein hits that are not upregulated in Alp-treated polyps compared to untreated controls. Table S1. The full list of proteins detected in the respective comparative analyses of the samples from wild-type AEP vs. HyActinP:HyWnt3 polyps and Alp-treated vs. DMSO-treated control polyps.

(F) WISH experiment using an LNA probe shows upregulated collar-like expression of *HAS-10* in gland cells of the upper gastric region of *Hydra*. Scale bar = 100 μm.

Wnt/β-catenin signaling acts on ECM remodeling

To unravel the molecular-level regulation of mesoglea elasticity during patterning, we performed a quantitative proteomic analysis of *Hydra* mesoglea by using Wnt/β-catenin-activated polyps. We compared two conditions with wild-type polyps: Alp-treated polyps and transgenic polyps overexpressing *Wnt3*. In contrast to Alp-treated polyps that transiently form ectopic tentacles, transgenic HyActinP:HyWnt3 *Hydra* constantly produces ectopic axes and head structures. We made use of this clear distinction to examine mesoglea factors that were upregulated in HyActinP:HyWnt3 polyps as compared to Alp-treated polyps. For this purpose, we performed comparative proteome analyses of mesoglea samples from wild-type AEP strain vs HyActinP:HyWnt3 polyps and Alp-treated vs DMSO-treated control polyps. The full list of proteins detected in the respective comparative analyses is presented in Table S1 (Table S1. The full list of proteins detected in the respective comparative analyses of the samples from wild-type AEP vs HyActinP:HyWnt3 polyps and Alp-treated vs DMSO-treated control polyps, related to Figure 5 and STAR Methods). We then selected for annotated protein hits that were exclusively upregulated in the transgenic Wnt3-overexpressing line but not in Alp-treated polyps (Figure 5E). Interestingly, this category of proteins contained several metalloproteases including HAS-10 astacin protease as well as several collagen molecules including Hcol-I (Figure 5E), indicating that axis formation induced by constant upregulation of β-catenin involves considerable remodeling and re-synthesis of core ECM factors. In addition, whole-mount *in situ* hybridization (WISH) for *HAS-10* showed a gradient-like expression pattern peaking below the tentacle zone (Figure 5F), which seems consistent with the elasticity patterns type B and type C. This strongly supports our hypothesis that the increase in the Young's modulus in the budding region of mature polyps originates from a gradient-like expression of proteases.

These changes in the elasticity patterns of *Hydra* mesoglea (ECM) during *Hydra* morphogenesis and their control by Wnt/β-catenin signaling were unexpected. They suggest, however, that tissue elasticity is necessary not only for the biomechanical integrity of the epithelia during growth but also for the more subtle processes of spatial and temporal integration of biochemical and biophysical signals in tissue morphogenesis.

DISCUSSION

The ECM in multicellular organisms serves as a cell substrate and as a medium for the transport of extracellular factors required for coordinated growth and patterning. Mounting evidence suggested that the remodeling of ECM, such as structural arrangement and modulation of ECM elasticity, is one of the prominent features in development and diseases.[1,46] In this study, we focused on how the patterns of ECM elasticity are spatio-temporally modulated in animals undergoing dynamic tissue morphogenesis. As a model, we have chosen the freshwater polyp *Hydra*, which is characterized by an enormous morphogenetic plasticity and regenerative capacity as well as an exceptional elasticity of its ECM compared to other animals.[47]

Biophysics of Hydra ECM reveal basis for its unique elasticity

Our structural analysis of *Hydra* ECM proteins by high resolution suggested that the micrometer-scale assemblies of HCol-I are region specific. The autocorrelation analysis of confocal images demonstrated that HCol-I bundles near the hypostome are aligned parallel, but this direction does not show any correlation with the body axis. On the other hand, the HCol-I bundles in middle and peduncle regions take distorted rectangular patterns. Intriguingly, in both regions, the characteristic spacing between the bundles aligned parallel to the OA axis (≈5 μm) is about one-half of those aligned almost perpendicular to the body axis (≈10 μm). This explains the fact that the body of *Hydra* can undergo significant stretching and contraction in the direction of the OA axis without inflating its cross-sectional area. Moreover, we found that the mesoglea of an evaginating bud showed no distinct features (Figure S4. Micrometer-scale order of

mesoglea of an evaginating bud, related to Figure 5) like the one from parental *Hydra*, which shows good agreement with previous account reporting the thinning of mesoglea during budding.[23]

In an in-depth analysis, we determined the nanometer-scale arrangement of ECM proteins using nano-GI-SAXS, which has been used mainly for colloids and polymers.[24,25] As nano-GISAXS enables one to collect the structural information from the beam footprint smaller than a mesoglea, we unraveled that collagen fibers (Hcol-I) take highly asymmetric, distorted hexagonal lattices. The packing of Hcol-I fibers along the body axis was found to be less ordered compared to the one perpendicular to the body axis, which can be attributed to an intrinsic body design of *Hydra* undergoing significant stretching and contraction along the oral-aboral axis. It is notable that the unit cell size of Hcol-I fibers is about 2–4 times larger compared to the standard samples from collagen type I fibers from rat tail tendon.[27,48,49] The apparently different packing of collagen fibers from vertebrates can be attributed to the amino acid composition. Compared to type I collagen from vertebrates, Hcol-I has a lower proline content and lacks typical lysine-crosslinking sites.[18] Moreover, an altered post-translational processing leads to the retention of the N-terminal pro-peptide-like domains,[18] resulting in weaker interfibrillar interactions between Hcol-I. It is remarkable that the collagen of *Hydra* ECM actually shares common structural features with Ehlers-Danlos syndrome characterized by the hypermobility of joints (which is claimed as the reason for extraordinary performance of Niccolo Paganini).[50,51]

Our data can explain the high tensile strength and mechanics of fibrillar collagens[51] reported before for *Hydra*.[21] Accordingly, HCol-I enabled *Hydra* mesoglea to be stretched even up to 7–8 times its length and twice its width, and it recovers the normal shape upon releasing the stress. Our proteome data showed that HCol-I contributes to a proportion of 6.1% of the total protein amount (Figure S5. Cumulative protein abundance vs. protein rank, related to Figure 5) and is among the ten highest abundant proteins (rank 5) of the mesoglea in steady-state AEP polyps (Table S2. Annotated list of the ten highest abundant proteins based on the Tandem Mass Tag (TMT) reporter ion signals of the AEP mesoglea samples, related to Figure 5.), which underscores its relevance for the mesoglea structure. Aufschnaiter et al. showed that *Hydra* mesoglea is continuously remodeled and moves toward both ends of the body column.[23] This displacement occurs largely in continuity with the epithelial cells that are secreting the ECM and is in accord with previous cell-labeling data from Campbell.[37,52]

Axial elasticity patterns of *Hydra* ECM are modulated by Wnt/β-catenin-mediated metalloprotease activity

We identified significant changes of ECM elasticity along the OA body axis. In the budding region, the parental mesoglea gets recruited and stretched by the evaginating bud without biosynthesis of new collagens at the early stages.[23] This suggests significant changes in the ECM elasticity in emerging buds. However, the cellular mechanisms of ECM remodeling and how ECM remodeling affects the biophysical properties of the ECM in space and in time during major morphological changes have so far remained unknown. By quantitative comparison of the elasticity patterns of mesoglea samples isolated from the synchronized culture by AFM nano-indentation, we unraveled the emergence of three characteristic "mechanical phenotypes" of *Hydra* mesoglea during tissue morphogenesis. After detachment from the parental polyp, the elastic moduli of the mesoglea from young polyps were low and uniform over the body axis (type A). The elasticity patterns of the mesoglea changed over 2–3 days, showing an increase in elastic moduli in a gradient-like fashion with a maximum in the budding region (types B/C) (Figure 4). This emergence of elasticity gradients from an initially uniform elasticity distribution over time seems plausible from the viewpoint of mechanics because the mature ECM of the budding region must mechanically support a rapidly growing bud possessing high local curvatures. On the other hand, from the viewpoint of protein biochemistry, the emergence of elasticity gradient clearly indicates either post-transcriptional modifications or changes in expression and composition of ECM proteins. As shown in Figure 5E, our proteomic data indicated distinct upregulations of several collagen molecules including HCol-I in *Wnt3*-overexpressing *Hydra* polyps. Notably, the proportion of HCol-I in *Wnt3*-overexpressing polyps was 7.4%, which is distinctly higher than that in wild-type polyps (6.1%) (Figure S5). On the other hand, several metalloproteases, such as HAS-10, also showed distinct upregulations in *Wnt3*-overexpressing polyps (Figure 5E). These data indicate that the axis formation induced by the constant activation of Wnt/β-catenin signaling involves both re-synthesis of core ECM factors and considerable remodeling by proteases. In contrast, Alp-treated polyps, in which Wnt/β-catenin signaling is upregulated only transiently, only produce ectopic tentacles but no ectopic body axis (Figure 5).
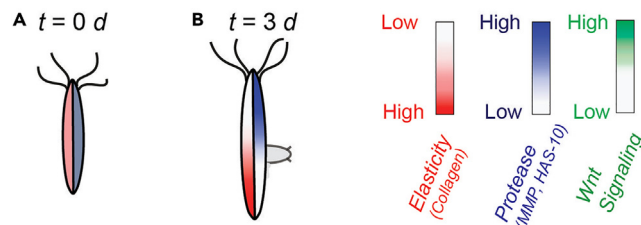
Figure 6. Spatiotemporal patterns of ECM elasticity and protease expression
(A) Freshly detached *Hydra* (*t* = 0 days) possesses uniform, soft mesoglea (type A), associated with uniformly high protease expression level.
(B) According to aging (*t* = 3 days), the downregulation in the budding region leads to the elevation of elastic moduli, resulting in type B/C patterns.

The proteome data of Alp-treated polyps showed an enrichment of basal lamina factors, such as laminin β subunit, but no distinct upregulation of metalloproteases was found as in Wnt3-overexpressing polyps (Table S1), although AFM measurements indicate a softening of the mesoglea in Alp-treated polyps (Figure 5B). This is most likely due to the transient induction of Wnt/β-catenin signaling and subsequent mesoglea turnover, which is difficult to detect by proteome analysis at a single time point after treatment (4 days).

When we silenced *HAS-10* expression by small interfering RNA (siRNA) electroporation, the ectopic tentacle formation (Table S3. Fraction of polyps with ectopic tentacles and the average number of ectopic tentacles in siHAS-10 and siGFP control polyps after Alp treatment, related to Figure 5) and the number of buds (Table S4. Number of buds in siHAS-10 and siGFP control animals, related to Figure 5) in Alp-treated polyps were only slightly affected, indicating redundant protease activity induced by Wnt/β-catenin and a compensation by other proteases after HAS10 knockdown. In fact, several astacin proteases were recently shown to be distinctly downregulated in the lower gastric region of polyps, while the expression levels remained high in the upper gastric region.[45] The softening of ECM in the peduncle region (type C pattern) can be explained by an upregulation of metalloprotease near the foot or bud.[10] This suggests that the modulation of elasticity patterns is induced by the combination of upregulation of fibrillar collagen and gradient-like expression of proteases.

It has been established that Wnt/β-catenin signaling plays central roles in axis formation of *Hydra*.[13] Other studies have also suggested that Wnt signaling induces the upregulation of metalloproteases in various developmental processes,[53–57] e.g., in embryonic neuronal stem cells,[58] in human mesenchymal stem cells, but also in the migration of single T cells[54] or in the collective migration of epithelial cells during would healing.[53] Therefore, we investigated whether the perturbation on Wnt/β-catenin pathway could influence the elasticity patterns in *Hydra* mesoglea by (a) treating wild-type polyps with Alp (Figure 5) and (b) using β-catenin- and Wnt3-overexpressing *Hydra* polyps (Figure S3). Alp is an inhibitor of GSKβ3, activating β-catenin all over the body column.[40,41] Both Alp-treated and β-catenin-overexpressing *Hydra* polyps exhibited significantly low elastic moduli all over the body column at *t* = 3 days. This is clearly different from the intact, wildt-ype *Hydra* exhibiting high elastic moduli in the budding region (type B/C). These results indicate that the modulation of elasticity patterns in mesoglea is tightly controlled by canonical Wnt signaling.

The next question one can address is whether the ECM stiffening coincides with the formation of highly curved structures, such as buds and tentacles. Several *in vitro* studies suggested that the collective cell migration, such as wound healing, is faster on stiffer substrates.[59,60] In case of budding *Hydra* polyps, the movement of cells into buds during the early budding stage is coupled to that of mesoglea, which is distinctly different from the normal migration caused by cell growth.[23] As presented in Figure S6 (Figure S6. Distribution of LifeAct GFP signals along the body axis of LifeAct ecto *Hydra* at *t* = 0 h, related to Figure 6), the stiffening of ECM is reflected by the increase in the actin filaments in the budding region. It is notable that such an unusual movement was also observed in tentacle-forming tissues.[23] Thus, one could hypothesize that bud and tentacle forming tissues might exhibit a similar elasticity level, if the increased Young's modulus of the mesoglea simply reflects the biomechanical constraints to support the evagination of highly curved structures. However, our Wnt perturbation results implied the opposite. The continuous activation of the Wnt pathway resulted in uniformly soft ECM along the entire body column (Figure S3), suggesting a

high level of protease activity (Figure 6) as previously shown for HAS-7 in *Wnt3*-overexpressing *Hydras*.[45] Thus, we concluded that there is no direct correlation between the ECM stiffening and evagination of highly curved tissues.

It is notable that the basement membrane factors like laminin were upregulated in the mesogleas of Alp-treated polyps (Table S1). This suggests that the formation of basement membrane precedes the synthesis of fibrillar ECM during head regeneration, as suggested previously.[12] We therefore presume that bud and tentacle formation reflects the early phase of regeneration in which epithelial cells re-align on the newly forming basement membrane. On the other hand, the synthesis of fibrillar ECM components in general is part of the late patterning phase triggered by β-catenin, as shown by the combined transcriptome and proteome analyses.[47]

Outlook: ECM elasticity and Hydra stem cells

Intriguingly, the gastric region, which is also characterized as the region where interstitial and epithelial stem cells show high activity and proliferation capacity, turns out to exhibit a highly dynamic landscape in terms of the biophysical properties of its ECM. Regions with lower or medium Young's moduli (i.e., the upper gastric region and the growing bud) are those regions that have a continuous and high proliferative capacity.[61] Currently, it is unclear whether these dynamic changes in ECM elasticity are also coupled to the stem cell functions of interstitial stem cells located in the upper and lower gastric region.[62,63] Further *in vitro* studies using substrates with tunable elasticity,[64,65] *in vivo* modulation of ECM elasticity,[9] and a genome-wide RNA tomography[66] along the OA axis of *Hydra* would help us unravel if the elasticity patterns in ECM are coupled to stem cell activities.

Limitations of the study

This study addresses the biophysical properties of isolated ECM/Mesoglea. Critical validation of these *ex vivo* data by *in vivo* data is obviously desirable but not experimentally possible. To test the extent to which the integrity of the ECM *ex vivo* corresponds to the *in vivo* situation, we performed a direct comparison of the distribution patterns of relevant ECM protein by immunofluorescence for collagen (Figures 1A and 1B) and laminin (Figure S1) under *in vivo* and *ex vivo* conditions. Both HCol-I and laminin show a completely intact mesoglea before and after de-cellularization. More detailed mapping with nano-GISAXS and spatial proteomics may yield further insights into the spatial variation of nanoscopic structural orders and protein-expression patterns along the body axis at higher resolution[67] but would not yield further information for the principal statement of this work, the relationship of Wnt signaling and the biophysical properties of the ECM.

Our proteomic data show a clear correlation between the gradient of metalloproteases with highest concentration at the oral end (such as HAS-10) and the activation of metalloproteases by the Wnt signaling pathway (Figure 5E and Table S1). Along with this, collagen formation is also activated (like Hcol-I). This suggests that axis formation is accompanied by substantial remodeling and re-synthesis of key ECM factors. At present, it remains open how the remodeling of mesoglea occurs in detail and which mettalo-proteases other than HAS-10 are involved. In any case, Wnt-mediated activation of metalloproteases leads to a dramatic decrease in ECM elasticity. It is therefore possible that the remodeling process involves not one metalloprotease but a "cocktail" of different metalloproteases. The use of broad metalloprotease inhibitors such as batimastat leads to corresponding pleiotropic and toxic effects. Further work is therefore needed to elucidate the specificity of the metalloproteases and their targets, which may explain the dramatic change in the biophysical properties of the ECM along the OA axis in Hydra and other Cnidaria.

STAR★METHODS

Detailed methods are provided in the online version of this paper and include the following:

- KEY RESOURCES TABLE
- RESOURCE AVAILABILITY
  - Lead contact
  - Materials availability
  - Data and code availability
- EXPERIMENTAL MODEL AND SUBJECT DETAILS
  - Animal studies
- METHOD DETAILS
  - Culture synchronization

- ○ Isolation of mesoglea
- ○ Immunofluorescence imaging
- ○ Nano-GISAXS experiments
- ○ Nano-GISAXS data analysis
- ○ Nano-indentation experiments
- ○ Sample preparation for mass spectroscopy
- ○ Mass spectrometry
- ○ siRNA electroporation
- ○ *In situ* hybridization
- ○ Alsterpaullone treatment
- ● QUANTIFICATION AND STATISTICAL ANALYSIS
  - ○ Autocorrelation analysis
  - ○ Nano-indentation analysis
  - ○ Elasticity pattern classification
  - ○ Mass spectroscopy data analysis

SUPPLEMENTAL INFORMATION

Supplemental information can be found online at https://doi.org/10.1016/j.isci.2023.106416.

AUTHOR CONTRIBUTIONS

M.T., T.W.H., and S.Ö designed and directed the research. M.V. and S.K. (Kling and Kaufmann) cultured polyps and prepared mesoglea samples. M.V., W.A., and M.B. measured nano-GISAXS, and M.V. and P.L. carried out AFM indentation. S.K. (Kling) and U.E. performed immunofluorescence imaging, and R.S. performed autocorrelation analysis and live imaging of *Hydra* polyps. H.P., S.K. (Kling), B.G.B., and F.S. performed mass spectrometry analysis. M.V., S.Ö., T.W.H., and M.T. wrote the manuscript, and all authors were involved in the discussion.

DECLARATION OF INTERESTS

The authors declare that they have no competing interests.

REFERENCES

1. Bonnans, C., Chou, J., and Werb, Z. (2014). Remodelling the extracellular matrix in development and disease. Nat. Rev. Mol. Cell Biol. *15*, 786–801. https://doi.org/10.1038/nrm3904.

2. Chaudhuri, O., Cooper-White, J., Janmey, P.A., Mooney, D.J., and Shenoy, V.B. (2020). Effects of extracellular matrix viscoelasticity on cellular behaviour. Nature *584*, 535–546. https://doi.org/10.1038/s41586-020-2612-2.

3. Dzamba, B.J., and DeSimone, D.W. (2018). Extracellular matrix (ECM) and the sculpting of embryonic tissues. Curr. Top. Dev. Biol. *130*, 245–274. https://doi.org/10.1016/bs.ctdb.2018.03.006.

4. Kraus, Y., and Technau, U. (2006). Gastrulation in the sea anemone Nematostella vectensis occurs by invagination and immigration: an ultrastructural study. Dev. Genes Evol. *216*, 119–132. https://doi.org/10.1007/s00427-005-0038-3.

5. Wallingford, J.B., Fraser, S.E., and Harland, R.M. (2002). Convergent extension: the molecular control of polarized cell movement during embryonic development. Dev. Cell *2*,

695–706. https://doi.org/10.1016/S1534-5807(02)00197-1.

6. Buesche, G., Teoman, H., Wilczak, W., Ganser, A., Hecker, H., Wilkens, L., Göhring, G., Schlegelberger, B., Bock, O., Georgii, A., and Kreipe, H. (2008). Marrow fibrosis predicts early fatal marrow failure in patients with myelodysplastic syndromes. Leukemia 22, 313–322. https://doi.org/10.1038/sj.leu.2405030.

7. Booth, A.J., Hadley, R., Cornett, A.M., Dreffs, A.A., Matthes, S.A., Tsui, J.L., Weiss, K., Horowitz, J.C., Fiore, V.F., Barker, T.H., et al. (2012). Acellular normal and fibrotic human lung matrices as a culture system for in vitro investigation. Am. J. Respir. Crit. Care Med. 186, 866–876. https://doi.org/10.1164/rccm.201204-0754OC.

8. Koser, D.E., Thompson, A.J., Foster, S.K., Dwivedy, A., Pillai, E.K., Sheridan, G.K., Svoboda, H., Viana, M., Costa, L.d.F., Guck, J., et al. (2016). Mechanosensing is critical for axon growth in the developing brain. Nat. Neurosci. 19, 1592–1598. https://doi.org/10.1038/nn.4394.

9. Barriga, E.H., Franze, K., Charras, G., and Mayor, R. (2018). Tissue stiffening coordinates morphogenesis by triggering collective cell migration in vivo. Nature 554, 523–527. https://doi.org/10.1038/nature25742.

10. Leontovich, A.A., Zhang, J., Shimokawa, K., Nagase, H., and Sarras, M.P. (2000). A novel hydra matrix metalloproteinase (HMMP) functions in extracellular matrix degradation, morphogenesis and the maintenance of differentiated cells in the foot process. Development 127, 907–920.

11. Shimizu, H., Zhang, X., Zhang, J., Leontovich, A., Fei, K., Yan, L., and Sarras, M.P. (2002). Epithelial morphogenesis in hydra requires de novo expression of extracellular matrix components and matrix metalloproteinases. Development 129, 1521–1532.

12. Bergheim, B.G., and Özbek, S. (2019). Extracellular matrix and morphogenesis in cnidarians: a tightly knit relationship. Essays Biochem. 63, 407–416. https://doi.org/10.1042/EBC20190021.

13. Holstein, T.W. (2022). The role of cnidarian developmental biology in unraveling axis formation and Wnt signaling. Dev. Biol. 487, 74–98. https://doi.org/10.1016/j.ydbio.2022.04.005.

14. Sarras, M.P., Jr., Madden, M.E., Zhang, X.M., Gunwar, S., Huff, J.K., and Hudson, B.G. (1991). Extracellular matrix (mesoglea) of Hydra vulgaris: I. Isolation and characterization. Dev. Biol. 148, 481–494. https://doi.org/10.1016/0012-1606(91)90266-6.

15. Sarras, M.P. (2012). Components, structure, biogenesis and function of the Hydra extracellular matrix in regeneration, pattern formation and cell differentiation. Int. J. Dev. Biol. 56, 567–576. https://doi.org/10.1387/ijdb.113445ms.

16. Lommel, M., Strompen, J., Hellewell, A.L., Balasubramanian, G.P., Christofidou, E.D., Thomson, A.R., Boyle, A.L., Woolfson, D.N., Puglisi, K., Hartl, M., et al. (2018). Hydra mesoglea proteome identifies thrombospondin as a conserved component active in head organizer restriction. Sci. Rep. 8, 11753. https://doi.org/10.1038/s41598-018-30035-2.

17. Shimizu, H., Aufschnaiter, R., Li, L., Sarras, M.P., Jr., Borza, D.-B., Abrahamson, D.R., Sado, Y., and Zhang, X. (2008). The extracellular matrix of hydra is a porous sheet and contains type IV collagen. Zoology 111, 410–418. https://doi.org/10.1016/j.zool.2007.11.004.

18. Deutzmann, R., Fowler, S., Zhang, X., Boone, K., Dexter, S., Boot-Handford, R.P., Rachel, R., and Sarras, M.P., Jr. (2000). Molecular, biochemical and functional analysis of a novel and developmentally important fibrillar collagen (Hcol-I) in hydra. Development 127, 4669–4680.

19. Zhang, X., Boot-Handford, R.P., Huxley-Jones, J., Forse, L.N., Mould, A.P., Robertson, D.L., Athiyal, M., Athiyal, M., and Sarras, M.P., Jr. (2007). The collagens of hydra provide insight into the evolution of metazoan extracellular matrices. J. Biol. Chem. 282, 6792–6802.

20. Hausman, R.E., and Burnett, A.L. (1970). The mesoglea of hydra. III. Fiber system changes in morphogenesis. J. Exp. Zool. 173, 175–185. https://doi.org/10.1002/jez.1401730206.

21. Hausman, R.E., and Burnett, A.L. (1969). The mesoglea of hydra. I. Physical and histochemical properties. J. Exp. Zool. 171, 7–13. https://doi.org/10.1002/jez.1401710103.

22. Burnett, A.L., and Hausman, R.E. (1969). Mesoglea of Hydra .2. Possible role in morphogenesis. J. Exp. Zool. 171, 15–23. https://doi.org/10.1002/jez.1401710104.

23. Aufschnaiter, R., Zamir, E.A., Little, C.D., Özbek, S., Münder, S., David, C.N., Li, L., Sarras, M.P., and Zhang, X. (2011). In vivo imaging of basement membrane movement: ECM patterning shapes Hydra polyps. J. Cell Sci. 124, 4027–4038. https://doi.org/10.1242/jcs.087239.

24. Roth, S.V., Autenrieth, T., Grübel, G., Riekel, C., Burghammer, M., Hengstler, R., Schulz, L., and Müller-Buschbaum, P. (2007). In situ observation of nanoparticle ordering at the air-water-substrate boundary in colloidal solutions using x-ray nanobeams. Appl. Phys. Lett. 91, 091915. https://doi.org/10.1063/1.2776850.

25. Roth, S.V., Rothkirch, A., Autenrieth, T., Gehrke, R., Wroblewski, T., Burghammer, M.C., Riekel, C., Schulz, L., Hengstler, R., and Müller-Buschbaum, P. (2010). Spatially resolved investigation of solution cast nanoparticle films by X-ray scattering and multidimensional data set classification. Langmuir 26, 1496–1500. https://doi.org/10.1021/la9037414.

26. Philipp, I., Aufschnaiter, R., Özbek, S., Pontasch, S., Jenewein, M., Watanabe, H.,

Rentzsch, F., Holstein, T.W., and Hobmayer, B. (2009). Wnt/β-Catenin and noncanonical Wnt signaling interact in tissue evagination in the simple eumetazoan Hydra. Proc. Natl. Acad. Sci. USA 106, 4290–4295. https://doi.org/10.1073/pnas.0812847106.

27. Wess, T.J., Hammersley, A., Wess, L., and Miller, A. (1995). Type I collagen packing, conformation of the triclinic unit cell. J. Mol. Biol. 248, 487–493. https://doi.org/10.1016/S0022-2836(95)80065-4.

28. Davis, L.E., and Haynes, J.F. (1968). An ultrastructural examination of the mesoglea of Hydra. Z. Zellforsch. Mikrosk. Anat. 92, 149–158. https://doi.org/10.1007/bf00335643.

29. Stolz, M., Raiteri, R., Daniels, A.U., VanLandingham, M.R., Baschong, W., and Aebi, U. (2004). Dynamic elastic modulus of porcine articular cartilage determined at two different levels of tissue organization by indentation-type atomic force microscopy. Biophys. J. 86, 3269–3283. https://doi.org/10.1016/S0006-3495(04)74375-1.

30. Liu, F., and Tschumperlin, D.J. (2011). Micro-mechanical characterization of lung tissue using atomic force microscopy. J. Vis. Exp.e2911. https://doi.org/10.3791/2911.

31. Long, Y., Cheddadi, I., Mosca, G., Mirabet, V., Dumond, M., Kiss, A., Traas, J., Godin, C., and Boudaoud, A. (2020). Cellular heterogeneity in pressure and growth emerges from tissue topology and geometry. Curr. Biol. 30, 1504–1516.e8. https://doi.org/10.1016/j.cub.2020.02.027.

32. Bilodeau, G.G. (1992). Regular pyramid punch problem. J. Appl. Mech. 59, 519–523.

33. Dimitriadis, E.K., Horkay, F., Maresca, J., Kachar, B., and Chadwick, R.S. (2002). Determination of elastic moduli of thin layers of soft material using the atomic force microscope. Biophys. J. 82, 2798–2810.

34. Lin, D.C., Dimitriadis, E.K., and Horkay, F. (2007). Robust strategies for automated AFM force curve analysis—I. Non-Adhesive indentation of soft, inhomogeneous materials. J. Biomech. Eng. 129, 430–440.

35. Bentele, T., Amadei, F., Kimmle, E., Veschgini, M., Linke, P., Sontag-González, M., Tennigkeit, J., Ho, A.D., Özbek, S., and Tanaka, M. (2019). New class of crosslinker-free nanofiber biomaterials from Hydra nematocyst proteins. Sci. Rep. 9, 19116. https://doi.org/10.1038/s41598-019-55655-0.

36. Otto, J.J., and Campbell, R.D. (1983). Marking epithelial cells in living hydra with Indian ink. In Hydra: Research Methods, H.M. Lenhoff, ed. (Springer), pp. 183–186.

37. Otto, J.J., and Campbell, R.D. (1977). Budding in Hydra attenuata: bud stages and fate map. J. Exp. Zool. 200, 417–428. https://doi.org/10.1002/jez.1402000311.

38. Lengfeld, T. (2009). Der Wnt/ß-Cateninsignalweg und die axiale Musterbildung im Süßwasserpolyp Hydra (PhD (Heidelberg University)).

39. Augustin, R., Franke, A., Khalturin, K., Kiko, R., Siebert, S., Hemmrich, G., and Bosch, T.C.G. (2006). Dickkopf related genes are components of the positional value gradient in Hydra. Dev. Biol. *296*, 62–70. https://doi.org/10.1016/j.ydbio.2006.04.003.

40. Guder, C., Pinho, S., Nacak, T.G., Schmidt, H.A., Hobmayer, B., Niehrs, C., and Holstein, T.W. (2006). An ancient Wnt-Dickkopf antagonism in Hydra. Development *133*, 901–911.

41. Broun, M., Gee, L., Reinhardt, B., and Bode, H.R. (2005). Formation of the head organizer in hydra involves the canonical Wnt pathway. Development *132*, 2907–2916. https://doi.org/10.1242/dev.01848.

42. Gufler, S., Artes, B., Bielen, H., Krainer, I., Eder, M.K., Falschlunger, J., Bollmann, A., Ostermann, T., Valovka, T., Hartl, M., et al. (2018). β-Catenin acts in a position-independent regeneration response in the simple eumetazoan Hydra. Dev. Biol. *433*, 310–323. https://doi.org/10.1016/j.ydbio.2017.09.005.

43. Nakamura, Y., Tsiairis, C.D., Özbek, S., and Holstein, T.W. (2011). Autoregulatory and repressive inputs localize Hydra Wnt3 to the head organizer. Proc. Natl. Acad. Sci. USA *108*, 9137–9142. https://doi.org/10.1073/pnas.1018109108.

44. Höger, S. (2017). Regeneration in Hydra. Die Rolle verschiedener Signalwege bei der Wiederherstellung des Hydra Kopforganisators (Heidelberg University).

45. Ziegler, B., Yiallouros, I., Trageser, B., Kumar, S., Mercker, M., Kling, S., Fath, M., Warnken, U., Schnölzer, M., Holstein, T.W., et al. (2021). The Wnt-specific astacin proteinase HAS-7 restricts head organizer formation in Hydra. BMC Biol. *19*, 120. https://doi.org/10.1186/s12915-021-01046-9.

46. Matsubayashi, Y. (2022). Dynamic movement and turnover of extracellular matrices during tissue development and maintenance. Fly *16*, 248–274. https://doi.org/10.1080/19336934.2022.2076539.

47. Petersen, H.O., Höger, S.K., Looso, M., Lengfeld, T., Kuhn, A., Warnken, U., Nishimiya-Fujisawa, C., Schnölzer, M., Krüger, M., Özbek, S., et al. (2015). A comprehensive transcriptomic and proteomic analysis of Hydra head regeneration. Mol. Biol. Evol. *32*, 1928–1947. https://doi.org/10.1093/molbev/msv079.

48. Hulmes, D.J., and Miller, A. (1979). Quasi-hexagonal molecular packing in collagen fibrils. Nature *282*, 878–880.

49. Orgel, J.P., Irving, T.C., Miller, A., and Wess, T.J. (2006). Microfibrillar structure of type I collagen in situ. Proc. Natl. Acad. Sci. USA *103*, 9001–9005. https://doi.org/10.1073/pnas.0502718103.

50. Sarras, M.P., Jr., and Deutzmann, R. (2001). Hydra and Niccolo Paganini (1782–1840)—two peas in a pod? The molecular basis of extracellular matrix structure in the invertebrate. Bioessays *23*, 716–724. https://doi.org/10.1002/bies.1101.

51. Sun, B. (2021). The mechanics of fibrillar collagen extracellular matrix. Cell Rep. Phys. Sci. *2*, 100515. https://doi.org/10.1016/j.xcrp.2021.100515.

52. Campbell, R.D. (1967). Tissue dynamics of steady state growth in Hydra littoralis. I. Patterns of cell division. Dev. Biol. *15*, 487–502.

53. Lyu, J., and Joo, C.K. (2005). Wnt-7a up-regulates matrix metalloproteinase-12 expression and promotes cell proliferation in corneal epithelial cells during wound healing. J. Biol. Chem. *280*, 21653–21660. https://doi.org/10.1074/jbc.M500374200.

54. Wu, B., Crampton, S.P., and Hughes, C.C.W. (2007). Wnt signaling induces matrix metalloproteinase expression and regulates T cell transmigration. Immunity *26*, 227–239. https://doi.org/10.1016/j.immuni.2006.12.007.

55. Kessenbrock, K., Dijkgraaf, G.J.P., Lawson, D.A., Littlepage, L.E., Shahi, P., Pieper, U., and Werb, Z. (2013). A role for matrix metalloproteinases in regulating mammary stem cell function via the Wnt signaling pathway. Cell Stem Cell *13*, 300–313. https://doi.org/10.1016/j.stem.2013.06.005.

56. Egea, V., Zahler, S., Rieth, N., Neth, P., Popp, T., Kehe, K., Jochum, M., and Ries, C. (2012). Tissue inhibitor of metalloproteinase-1 (TIMP-1) regulates mesenchymal stem cells through let-7f microRNA and Wnt/beta-catenin signaling. Proc. Natl. Acad. Sci. USA *109*, E309–E316. https://doi.org/10.1073/pnas.1115083109.

57. Zhou, L., and Liu, Y. (2015). Wnt/β-catenin signalling and podocyte dysfunction in proteinuric kidney disease. Nat. Rev. Nephrol. *11*, 535–545. https://doi.org/10.1038/nrneph.2015.88.

58. Ingraham, C.A., Park, G.C., Makarenkova, H.P., and Crossin, K.L. (2011). Matrix metalloproteinase (MMP)-9 induced by Wnt signaling increases the proliferation and migration of embryonic neural stem cells at low O2 levels. J. Biol. Chem. *286*, 17649–17657. https://doi.org/10.1074/jbc.M111.229427.

59. Balcioglu, H.E., Balasubramaniam, L., Stirbat, T.V., Doss, B.L., Fardin, M.-A., Mège, R.M., and Ladoux, B. (2020). A subtle relationship between substrate stiffness and collective migration of cell clusters. Soft Matter *16*, 1825–1839. https://doi.org/10.1039/C9SM01893J.

60. Ng, M.R., Besser, A., Danuser, G., and Brugge, J.S. (2012). Substrate stiffness regulates cadherin-dependent collective migration through myosin-II contractility. J. Cell Biol. *199*, 545–563. https://doi.org/10.1083/jcb.201207148.

61. Holstein, T.W., Hobmayer, E., and David, C.N. (1991). Pattern of epithelial cell cycling in hydra. Dev. Biol. *148*, 602–611. https://doi.org/10.1016/0012-1606(91)90277-A.

62. Bosch, T.C.G. (2009). Hydra and the evolution of stem cells. Bioessays *31*, 478–486. https://doi.org/10.1002/bies.200800183.

63. Watanabe, H., Hoang, V.T., Mättner, R., and Holstein, T.W. (2009). Immortality and the base of multicellular life: lessons from cnidarian stem cells. Semin. Cell Dev. Biol. *20*, 1114–1125. https://doi.org/10.1016/j.semcdb.2009.09.008.

64. Frank, V., Kaufmann, S., Wright, R., Horn, P., Yoshikawa, H.Y., Wuchter, P., Madsen, J., Lewis, A.L., Armes, S.P., Ho, A.D., and Tanaka, M. (2016). Frequent mechanical stress suppresses proliferation of mesenchymal stem cells from human bone marrow without loss of multipotency. Sci. Rep. *6*, 24264. https://doi.org/10.1038/srep24264.

65. Kidoaki, S. (2019). Frustrated differentiation of mesenchymal stem cells. Biophys. Rev. *11*, 377–382. https://doi.org/10.1007/s12551-019-00528-z.

66. Junker, J.P., Noël, E.S., Guryev, V., Peterson, K.A., Shah, G., Huisken, J., McMahon, A.P., Berezikov, E., Bakkers, J., and van Oudenaarden, A. (2014). Genome-wide RNA tomography in the zebrafish embryo. Cell *159*, 662–675. https://doi.org/10.1016/j.cell.2014.09.038.

67. Moffitt, J.R., Lundberg, E., and Heyn, H. (2022). The emerging landscape of spatial profiling technologies. Nat. Rev. Genet. *23*, 741–759. https://doi.org/10.1038/s41576-022-00515-3.

68. Perez-Riverol, Y., Bai, J., Bandla, C., García-Seisdedos, D., Hewapathirana, S., Kamatchinathan, S., Kundu, D.J., Prakash, A., Frericks-Zipper, A., Eisenacher, M., et al. (2022). The PRIDE database resources in 2022: a hub for mass spectrometry-based proteomics evidences. Nucleic Acids Res. *50*, D543–D552.

69. Wong, W.Y., Simakov, O., Bridge, D.M., Cartwright, P., Bellantuono, A.J., Kuhn, A., Holstein, T.W., David, C.N., Steele, R.E., and Martínez, D.E. (2019). Expansion of a single transposable element family is associated with genome-size increase and radiation in the genus Hydra. Proc. Natl. Acad. Sci. USA *116*, 22915–22917. https://doi.org/10.1073/pnas.1910106116.

70. Martin, V.J., Littlefield, C.L., Archer, W.E., and Bode, H.R. (1997). Embryogenesis in hydra. Biol. Bull. *192*, 345–363.

71. Lenhoff, H.M., and Brown, R.D. (1970). Mass culture of hydra: an improved method and its application to other aquatic invertebrates. Lab. Anim. *4*, 139–154. https://doi.org/10.1258/002367770781036463.

72. Shostak, S., Patel, N.G., and Burnett, A.L. (1965). The role of mesoglea in mass cell movement in Hydra. Dev. Biol. *12*, 434–450. https://doi.org/10.1016/0012-1606(65)90008-4.

73. Schindelin, J., Arganda-Carreras, I., Frise, E., Kaynig, V., Longair, M., Pietzsch, T., Preibisch, S., Rueden, C., Saalfeld, S., Schmid, B., et al. (2012). Fiji: an open-source platform for biological-image analysis. Nat. Methods *9*, 676–682.

74. Ponchut, C., Rigal, J.M., Clément, J., Papillon, E., Homs, A., and Petitdemange, S. (2011). MAXIPIX, a fast readout photon-counting X-ray area detector for synchrotron applications. J. Instrum. 6, C01069.

75. Schneider, C.A., Rasband, W.S., and Eliceiri, K.W. (2012). NIH Image to ImageJ: 25 years of image analysis. Nat. Methods 9, 671–675.

76. Reichel, M., Liao, Y., Rettel, M., Ragan, C., Evers, M., Alleaume, A.-M., Horos, R., Hentze, M.W., Preiss, T., and Millar, A.A. (2016). Planta determination of the mRNA-binding proteome of arabidopsis etiolated seedlings. Plant Cell 28, 2435–2452. https://doi.org/10.1105/tpc.16.00562.

77. Hughes, C.S., Moggridge, S., Müller, T., Sorensen, P.H., Morin, G.B., and Krijgsveld, J. (2019). Single-pot, solid-phase-enhanced sample preparation for proteomics experiments. Nat. Protoc. 14, 68–85. https://doi.org/10.1038/s41596-018-0082-x.

78. Hughes, C.S., Foehr, S., Garfield, D.A., Furlong, E.E., Steinmetz, L.M., and Krijgsveld, J. (2014). Ultrasensitive proteome analysis using paramagnetic bead technology. Mol. Syst. Biol. 10, 757. https://doi.org/10.15252/msb.20145625.

79. Domke, J., and Radmacher, M. (1998). Measuring the elastic properties of thin polymer films with the atomic force microscope. Langmuir 14, 3320–3325. https://doi.org/10.1021/la9713006.

80. Ritchie, M.E., Phipson, B., Wu, D., Hu, Y., Law, C.W., Shi, W., and Smyth, G.K. (2015). Limma powers differential expression analyses for RNA-sequencing and microarray studies. Nucleic Acids Res. 43, e47. https://doi.org/10.1093/nar/gkv007.

81. Huber, W., von Heydebreck, A., Sültmann, H., Poustka, A., and Vingron, M. (2002). Variance stabilization applied to microarray data calibration and to the quantification of differential expression. Bioinformatics 18, S96–S104. https://doi.org/10.1093/bioinformatics/18.suppl_1.S96.

82. Naba, A., Clauser, K.R., Hoersch, S., Liu, H., Carr, S.A., and Hynes, R.O. (2012). The matrisome: in silico definition and in vivo characterization by proteomics of normal and tumor extracellular matrices. Mol. Cell. Proteomics 11. M111.014647. https://doi.org/10.1074/mcp.M111.014647.

STAR★METHODS

KEY RESOURCES TABLE

REAGENT or RESOURCE	SOURCE	IDENTIFIER
Antibodies		
mAb52 raised against Hydra laminin	Xiaoming Zhang Lab, University of Kansas Medical Center	N/A
mAb39 raised against HCol-I	Xiaoming Zhang Lab, University of Kansas Medical Center	N/A
Goat anti-Mouse IgG (H+L) Cross-Adsorbed Secondary Antibody, Alexa Fluor™ 488	Thermo-Fisher	Cat# A-11001, RRID: AB_2534069
Alkaline phosphatase (AP)-conjugated anti-DIG antibody	Roche	Cat# 11093274910, RRID: AB_514497
Chemicals, peptides, and recombinant proteins		
Alsterpaullone	Sigma-Aldrich	Cat# A4847
Blocking Reagent	Roche	Cat# 11096176001
Bovine serum albumin	Sigma-Aldrich	Cat# A-9647
$CaCl_2$	Carl Roth	Cat# 5239.1
CHAPS	Sigma-Aldrich	Cat# C3023
cOmplete™ ULTRA Tablets, Mini, EASYpack Protease Inhibitor Cocktail	Roche	Cat# 05892970001
D-(+)-Glucose	Sigma-Aldrich	Cat# G8270
Denhardt's Solution	Sigma-Aldrich	Cat# D2532
Dimethyl sulfoxide	Sigma-Aldrich	Cat# D8418
Ficoll® Paque Plus	Sigma-Aldrich	Cat# GE17-1440-02
Gelatin	Dr. Oetker GmbH	N/A
Glutaraldehyde	Sigma-Aldrich	Cat# G5882
Glycerol	VWR Chemicals	Cat# ACRO259772500
Heparin sodium salt from porcine intestinal mucosa	Sigma-Aldrich	Cat# H3149
Kanamycin	Sigma-Aldrich	Cat# K0254
KCl	Sigma-Aldrich	Cat# P9541
MgSO4	Sigma-Aldrich	Cat# M7506
Mowiol	Sigma-Aldrich	N/A
N-Laurylsarcosine	Sigma-Aldrich	Cat# 61739
NaCl	neoFroxx GmbH	N/A
NBT-BCIP® solution	Roche	Cat# 72091
Paraformaldehyde	Carl Roth	N/A
Polyvinylpyrrolidone	Sigma-Aldrich	Cat# PVP40
Rifampicin	Sigma-Aldrich	Cat# R3501
RNA from yeast	Roche	Cat# 10109223001
Sodium citrate	Sigma-Aldrich	Cat# 1613859
Sodium pyruvate	Sigma-Aldrich	Cat# P2256
Streptomycin	Sigma-Aldrich	Cat# 85886
Sucrose	Sigma-Aldrich	Cat# 1.07653
TES	Carl Roth	Cat# 9137.1

Continued

REAGENT or RESOURCE	SOURCE	IDENTIFIER
Triethanolamine	Sigma-Aldrich	Cat# T58300
Tween®-20	Sigma-Aldrich	Cat# 8.17072
Critical commercial assays		
Plasmid Mini Kit	QIAGEN	Cat# 12123
Plasmid Midi Kit	QIAGEN	Cat# 12143
Deposited data		
Proteomics data at PRIDE	https://www.ebi.ac.uk/pride/	PRIDE: PXD039846
Experimental models: Organisms/strains		
Hydra vulgaris AEP	Thomas Bosch lab, University of Kiel, Germany	N/A
Hydra vulgaris overexpressing *Wnt3* (*HyActP::HyWnt3*)	Holstein Lab	N/A
Hydra vulgaris AEP Act::GFPectoderm/Act::RFPendoderm	Dr. Robert Steele, University of Caifornia, Irvine	N/A
Hydra vulgaris overexpressing *β-catenin* (*Hyβ-catenin::β-catenin-GFP*)	Holstein Lab	N/A
Artemia salina nauplii	Tropic Marine	N/A
Oligonucleotides		
LNA digoxygenin-labeled RNA probe to the antisense strand of the *HAS-10* cDNA: TACTGTACCAAGTCGCAAGCAA	Qiagen, Hilden, Germany	N/A
siRNA targeting sequences: HAS-10: 1. AAACACACAAATTGTATTAAA 2. AATACGTCATTGTTCCAGGAT 3: AATCATCACTCTAAACAAAGA	Sigma-Aldrich	N/A
siRNA targeting sequence: GFP: AAGGUGAUGCAACAUACGGAA	Sigma-Aldrich	N/A
Software and algorithms		
Image J version 2.1.0/1.53c	Open-source image processing software	https://imagej.nih.gov/ij/ RRID:SCR_003070
Bio-formats plugin (FIJI)	Opensource	RRID:SCR_000450
MATLAB	Mathworks, MA, USA	N/A
NIS elements Imagine software	Nikon Instruments Inc.	https://www.microscope.healthcare.nikon.com/products/software/nis-elements
Photoshop CS6 23.5.0	Adobe	https://www.adobe.com
Adobe Illustrator 26.5	Adobe	https://www.adobe.com
Microsoft Word version 16.64	Microsoft	https://www.microsoft.com/
Microsoft excel version 16.63.1	Microsoft	RRID:SCR_016137; https://www.microsoft.com/
Prism 9	Graphpad	https://www.graphstats.net/
Other		
Siliconnitride widow with Si frame for nano-GISAXS	SPI Supplies, West Chester, US	Cat# 4129SN-BA
AFM tip for indentation	Bruker, Karlsruhe, Germany	MLCT
Pasteur capillary pipettes	neoLab Migge	N/A
KL1500 HAL Light source for stereo microscopy	Schott AG	N/A
Microscope slide 76x26 mm	neoLab Migge	N/A

(Continued on next page)

Continued

REAGENT or RESOURCE	SOURCE	IDENTIFIER
Cover slips 24x32 mm	Paul Marienfeld	N/A
Nikon A1R Confocal Laser Scanning Microscope	Nikon A1R Confocal Laser Scanning Microscope	RRID:SCR_020317
Nikon Eclipse 80i microscope	Nikon Eclipse 80i Advanced Research Microscope	RRID:SCR_015572
Gene Pulser® Cuvette, 0.4 cm electrode gap	Bio-Rad	Cat# 1652088
GenePulser XcellTM	Bio-Rad	Cat# 1652660

RESOURCE AVAILABILITY

Lead contact

Further information and requests for resources should be directed to and will be fulfilled by the lead contact, Motomu Tanaka (tanaka@uni-heidelberg.de).

Materials availability

Further information and requests for reagents and materials should be directed to and will be fulfilled by the lead contact, Motomu Tanaka (tanaka@uni-heidelberg.de).

Data and code availability

- The mass spectrometry proteomics data have been deposited to the ProteomeXchange Consortium via the PRIDE partner repository,[68] and accession number is listed in the key resources table.

- This paper does not report original code.

- Any additional information required to reanalyze the data reported in this paper is available from the lead contact upon request.

EXPERIMENTAL MODEL AND SUBJECT DETAILS

Animal studies

Polyps of the *Hydra vulgaris* AEP strain[69,70] and transgenic lines[43] were cultured in modified *Hydra* medium[71] (1.0 mM $CaCl_2$, 1.0 mM Tris-HCl, 1.0 mM $NaHCO_3$, 0.1 mM KCl, 0.1 mM $MgCl_2$, pH = 7.4) and kept at $(18 \pm 0.5)°C$. Before mesoglea isolation, the culture was synchronized. Polyps were fed daily with *Artemia* and cleaned a few hours after feeding. The details of strains used in this study are listed in the key resources table.

METHOD DETAILS

Culture synchronization

Hydras with buds at different developmental stages were collected from a culturing box, which was fed for at least 2–3 weeks on a daily base and transferred to 24-well-plates (1 *Hydra*/ well). The detachment of new buds from collected *Hydra* polyps was checked twice a day. To obtain a synchronized culture the freshly detached buds were collected and transferred to new 24-well-plates (1 *Hydra*/ well). The day of detachment was defined as $t = 0$ d.

Isolation of mesoglea

Hydra polyps were starved for 1 d and transferred to a 2 ml test tube with *Hydra* medium (1 *Hydra* per tube). *Hydra* medium was replaced by 1.5 ml of a 0.5% w/v solution of N-lauroylsarcosine sodium salt in water. The sample was then immersed in liquid nitrogen for 10 min. Frozen polyp samples were either used directly or stored at $-80°C$. To extract the mesoglea, polyps were transferred to distilled water after thawing and forced through a Pasteur pipette 20 to 40 times. The washing water was exchanged 3 times. Subsequently, the isolated mesoglea was transported to a dry Petri dish with a drop of water and allowed to dry overnight at room temperature. Large numbers of mesogleas were isolated by a modification of the method used by Shostak et al.[72] In order to inhibit proteolytic degradation during isolation, Protease inhibitor cocktail

tablets (cOpmlete Ultra tablets, mini, *EASYpack*, Roche, Switzerland) were used according to the procedure protocol provided by the supplier. Pellets of 90–150 frozen *Hydra* animals were transferred to protease inhibitor cocktail and allowed to thaw at room temperature. After thawing, *Hydra* animals were transferred to a glass test tube with 3–4 mL protease inhibitor cocktail, and cells were removed by successive pipetting using a Pasteur pipette. Subsequently 1–2 ml of 80% sucrose solution were gently injected below the suspension to prevent the mesogleas from sticking to the glass bottom. The mixture was then centrifuged at 4°C and 300 g for 5 min using a swing-out bucket rotor. After centrifugation mesogleas were collected from the sucrose-water interface. The procedure was repeated 7–10 times.

Immunofluorescence imaging

Isolated mesogleas were mounted on gelatine-coated slides (5% gelatine in H_2O) by letting the mesoglea sink and stick onto the gelatine/coated glass. After washing, the immunofluorescence staining was conducted by incubating the samples with monoclonal HCol-I (mAb39) at 1:500 or laminin (mAb52) antibody at 1:100 for 60 min at room temperature or overnight at 4°C.[17] Samples were washed twice for 15 min in PBS-T, and then incubated with a fluorophore-conjugated secondary antibody (Alexa 488 anti mouse (Thermo Fisher Inc., Karlsruhe, Germany). After additional 3 washes in PBS-T, the PBS-T was removed and replaced with 50 vol% glycerol (VWR Chemicals, Darmstadt, Germany) in PBS and the slides were sealed with a coverslip and nail polish. Images were acquired with a Nikon A1 confocal microscope (Nikon Europe, Düsseldorf, Germany). For close-up images a Nikon 60× water objective was used. Images were analyzed using the NIS Elements software. All images were analyzed using Fiji software,[73] merging hyperstacks onto one plane.

Nano-GISAXS experiments

Nano-GISAXS experiments were performed at the European Synchrotron Radiation Facility (ESRF) beamline ID13 (Grenoble, France). Mesoglea samples were prepared 2–3 d before experiments and deposited on a 100 nm-thick Si_3N_4 window surrounded by a Si frame (SPI Supplies PA, US). Experiments were performed on dehydrated samples and at $T = 20°C$ and ambient pressure. Mesoglea samples were probed with nano-focused beam (diameter: 200 nm) with a wavelength of 0.81 Å (15.3 keV) and at an incident angle of 0.46°. Data was collected with a 2D detector (Maxipix, ESRF, France).[74] Silver behenate ($C_{21}H_{43}COOAg$) was used for calibration.

Nano-GISAXS data analysis

After background subtraction and deadtime correction satellite peak positions were determined using 2D-gaussian fit. The error was estimated by the half width at half maximum. The angle was determined from the dot product of reciprocal space vectors according to

$$\cos \gamma^* = \frac{\overrightarrow{a^*} \cdot \overrightarrow{b^*}}{\left|\overrightarrow{a^*}\right|\left|\overrightarrow{b^*}\right|} \qquad \text{(Equation 1)}$$

where a^* and b^* represent the reciprocal lattice vectors with an angle of γ^*. The angle in real space, γ, was calculated as

$$\gamma = \pi - \gamma^* \qquad \text{(Equation 2)}$$

The real lattice vectors were determined using $\overrightarrow{a} \cdot \overrightarrow{a^*} = 2\pi$ and $\overrightarrow{b} \cdot \overrightarrow{b^*} = 2\pi$.

Nano-indentation experiments

Nano-indentation was performed utilizing a JPK-NanoWizard3 atomic force microscope (JPK, Berlin, Germany) mounted on a Zeiss Axiovert 200 microscope (Zeiss, Oberkochen, Germany). Silicon nitride Cantilevers with a nominal spring constant of 10 mN/m and tip-radius of 20 nm were used (MLCT-Probes, Bruker, Karlsruhe, Germany). Indentation experiments were carried out in 150 mM NaCl. The spring constant of each cantilever was determined prior to measurements using the thermal noise method. A total number of $n = 38$ *Hydra* polyps out of a daily fed synchronized culture were examined. *Hydra* samples were between 0 and 10 d old and bore no more than 3 buds. Depending on the size, each mesoglea was indented at 7–37 different positions along the body column. Mesoglea was indented with a speed of 2–6 µm/s and up to a cantilever deflection of 0.8 V relative to the baseline. At each position along the *Hydra* body axis 4 points with a distance of 5 µm were indented. Each spot was indented two times. Subsequent

measurements at the same spot with a standard deviation larger than 10% were discarded. Local elastic moduli at each position on mesoglea were determined by averaging over the 8 measurements. Data points with standard deviation larger than 40% were discarded. The relative measurement position was determined using ImageJ.[75]

Sample preparation for mass spectroscopy

Isolated mesogleas (n ≥ 20) from AEP, ActP:Wnt3a, Alp-treated AEP (4 days after treatment) and DMSO-treated AEP hydras (4 days after treatment) were purified for protein content by trichloroacetic acid (TCA) precipitation. For SP3 and TMT labelling, TCA pellets were mixed with 50 µl of 1% SDS (in 50 mM HEPES, pH 8.5), vortexed and sonicated for 5 min. Reduction and alkylation was performed as described before.[76] Samples were further prepared using the SP3 protocol.[77] Trypsin (sequencing grade, Promega) was added to the samples in an enzyme to protein ratio 1:50 and digested overnight at 37°C. Then, peptide recovery was performed in HEPES buffer. The supernatant was collected on a magnet and combined with the second elution wash of beads with HEPES buffer. The samples were then labeled with TMT6plex Isobaric Label Reagent (ThermoFisher) according to the manufacturer's instructions. Briefly, 42 µl acetonitrile (100%) were added to 0.8 mg reagent and dissolved, then 4 µl of stock was added and incubated for 1 h at RT, followed by quenching the reaction with 5% hydroxylamine for 15 min at RT. Samples were pooled for the TMT10plex. An OASIS® HLB µElution Plate (Waters) was used for further sample purification. The offline high pH reverse phase fractionation was performed on an Agilent 1200 Infinity high-performance liquid chromatography system with a Gemini C18 column (3 µm, 110 Å, 100 × 1.0 mm, Phenomenex).[76]

Mass spectrometry

Proteome samples were prepared and analyzed as described in Supporting Information. For the transgenic and experimentally treated *Hydra vulgaris* (AEP strain), extracted mesoglea of polyps was isolated, proteins were prepared for the SP3 and TMT labelling approach.[77,78] Peptides were analyzed on an UltiMate 3000 RSLC nano LC system (Dionex) and QExactive plus (Thermo) mass spectrometer. All annotated protein identifiers were aligned with known *Hydra vulgaris* proteins (*H. magnipapillata* 105 strain).

siRNA electroporation

siRNA electroporation was performed as described previously.[45] An equimolar mixture of three *HAS-10* siRNAs combined with siGFP (3 µM in total) was used for the knockdown of the target mRNA, while 3 µM siGFP was used as the control. The movement of electroporated polyps was minimized during daily feeding and medium changes. The treatment with a low-dose Alp was performed 7 d after electroporation. The fraction of animals showing ectopic tentacles as well as the number of ectopic tentacles of each polyp were counted 4 d after the Alp treatment, and the number of were counted 13 d after electroporation. The used siRNA sequences are as follows. HAS-10 siRNA 1: AAACACACAAATTGTATTAAA; HAS-10 siRNA 2: AATACGTCATTGTTCCAGGAT; HAS-10 siRNA 3: AATCATCACTCTAAACAAAGA; siGFP: AAGGUGAUG CAACAUACGGAA.

In situ hybridization

A customized LNA digoxygenin-labeled RNA probe was designed and produced by Qiagen corresponding to the antisense strand of the *HAS-10* cDNA (TACTGTACCAAGTCGCAAGCAA). The whole-mount ISH procedure was performed as described previously in Ziegler et al.[45] Samples were finally mounted in PBS containing 90% glycerol, or in Mowiol 4–88 (Carl Roth), and images were acquired with a Nikon Digital Sight DS-U1 camera mounted on Nikon Eclipse 80i and imaging software NIS Elements (3.10, SP3, Hotfix, Build645). Further image processing was performed with Adobe Photoshop CS6 and Fiji.[73]

Alsterpaullone treatment

Freshly detached buds collected from a synchronized culture were incubated in a 5 µM solution of alsterpaullone (Sigma-Aldrich, United States) in 0.025% dimethyl sulfoxide (Sigma-Aldrich, United States) in *Hydra* medium for 1 d. Subsequently, polyps were washed several times with *Hydra* medium and cultured for up to 4 d.

QUANTIFICATION AND STATISTICAL ANALYSIS

Autocorrelation analysis

For an image *I* of size $m \times n$, autocorrelation G can be calculated as

$$G(a, b) = \sum_{x}^{m} \sum_{y}^{n} i(x, y) * i(x - a, y - b), \qquad \text{(Equation 3)}$$

where $i(x,y)$ is the image intensity at position (x,y), and a and b represent the distance (or lag) from the corresponding x and y position. From a practical viewpoint, calculating the autocorrelation using Equation 3 is computationally intensive. Hence, autocorrelation of an image was extracted via fast Fourier transforms using the Weiner-Khinchin theorem as

$$G(a, b) = \mathcal{F}^{-1}\left\{ |\mathcal{F}(I)|^2 \right\}, \qquad \text{(Equation 4)}$$

where $\mathcal{F}$ and $\mathcal{F}^{-1}$ are the fast Fourier transform and inverse fast Fourier transform, respectively. The autocorrelation analysis was performed with MATLAB (MathWorks, MA, US) using a self-written algorithm.

Nano-indentation analysis

The bulk elastic modulus E was calculated with the modified Hertz model[32]:

$$(z - z_0) = (d - d_0) - \sqrt{\frac{2(1 - v^2)k(d - d_0)}{1.4906\, E \tan \varphi}} \qquad \text{(Equation 5)}$$

z is position of the tip, d cantilever deflection. z_0 and d_0 are the values corresponding to the first tip-sample contact. v is Poisson's ratio (0.5), k the spring constant of the cantilever, and φ the half-opening angle of the AFM tip. To determine the elastic modulus, we have the contact point candidates "march" and applied the algorithm by Lin et al.[34] and Dimitriadis et al.[33] The minimization of mean sum of square residuals (SSR) yielded the best-fit result (Figure 3). To avoid the thickness-dependent mis-estimation of the Young's modulus,[79] the fitting range was kept within 10% of the total thickness of the mesoglea (Figure S7. Thickness of isolated Hydra mesoglea determined from confocal images, related to Figure 3.). Data in the figures are presented as means and standard deviations.

The onset point of each force curve was chosen as the center of the marching range. This point was determined roughly by fitting linear functions to the outermost parts of the noncontact and contact region of a force curve given by following relations, respectively:

$$r_{noncontact} = \left\{ (z, d) \in data \left| \frac{(z_{min} + z_{max})}{2} < z \right. \right\} \qquad \text{(Equation 6)}$$

$$r_{contact} = \left\{ (z, d) \in data \left| \frac{(d_{min} + d_{max})}{2} < d \right. \right\} \qquad \text{(Equation 7)}$$

where z and d corresponds to the piezo and deflection of a datapoint, z_{max} and z_{min} corresponds to the maximum and minimum piezopositions and d_{max} and d_{min} represent the maximum and minimum cantilever deflection in the dataset. Subsequently, the data point nearest to the intersection of the two fitted lines was defined as the center of marching range (z_c, d_c). All datapoint within a specific radius R from the inflection point were assigned to the marching range.

$$s_{marching} = \left\{ (z, d) \in data \left| \sqrt{(z - z_c)^2 + (d - d_c)^2} \leq R \right. \right\} \qquad \text{(Equation 8)}$$

The radius was adjusted according to the force curves so that the points at the beginning and end of the marching range were definitly far from the transition from contact to non-contact region.

Elasticity pattern classification

Average elastic moduli of upper gastric region ($0.6 \leq d \leq 1.0$), and peduncle ($0.0 \leq d < 0.1$) were normalized by the elastic modulus of the budding region ($0.1 \leq d \leq 0.3$). The distribution of $E_{gastric}/E_{budding}$ and $E_{peduncle}/E_{budding}$ are shown in Figure S2. Each histogram could be fitted with a sum of two Gaussians. In case of $E_{gastric}/E_{budding}$ the two Gaussians intersected at $E_{gastric}/E_{budding} = 0.71$ (Figure S2A). This value was taken as the threshold to discrimination between Type A and Type B/C: elasticity maps with $E_{gastric}/E_{budding} \geq 0.71$ were considered as uniformly elastic, i.e. type A patterns. The remaining patterns were compared with regard to the elasticity of peduncle relative to budding region, i.e., $E_{peduncle}/E_{budding}$. In this case the intersection point of the fitted Gaussians found at $E_{peduncle}/E_{budding} = 0.85$ (Figure S2B)

served as a criterion for discrimination between pattern B, with $E_{peduncle}/E_{budding} \geq 0.85$, and pattern C with $E_{peduncle}/E_{budding} < 0.85$.

Mass spectroscopy data analysis

For LC-MS/MS, Liquid Chromatography (LC) was performed on an UltiMate 3000 RSLC nano LC system (Dionex) fitted with a trapping cartridge (μ-Precolumn C18 PepMap 100, 5 μm, 300 μm i.d. x 5 mm, 100 Å) and an analytical column (nanoEase™ M/Z HSS T3 column 75 μm × 250 mm C18, 1.8 μm, 100 Å, Waters). For trapping, a constant flow of 0.05% trifluoroacetic acid at 30 μL/min onto the trapping column for 6 min was used. Peptide elution was carried out on an analytical column with a constant flow of solvent A (0.1% formic acid in water) at 0.3 μL/min, and an increasing percentage of solvent B (0.1% formic acid in acetonitrile) from 2% to 4% in 4 min, from 4% to 8% in 2 min, then 8%–28% for a further 66 min, and finally from 28% to 40% in another 10 min. The outlet of the 33 analytical column was coupled directly to a QExactive plus (Thermo) mass spectrometer using the proxeon nanoflow source in positive ion mode. The peptides were added to the QExactive plus via a Pico-Tip Emitter 360 μm OD x 20 μm ID; 10 μm tip (New Objective) with a spray voltage of 2.2 kV. Full mass scan was acquired with mass range 375–1200 m/z in profile mode with a resolution of 70000, a capillary temperature of 275°C and a filling time of maximal 100 ms with a limitation of $3x10^6$ ions. Data dependent acquisition (DDA) was carried out with the resolution of the Orbitrap set to 17500, with a fill time of 50 ms and a limitation of $2x10^5$ ions. A normalized collision energy of 32 was used. Dynamic exclusion time of 20 s was applied. The peptide match algorithm was set to 'preferred' and charge exclusion 'unassigned', charge states 1, 5–8 were excluded. MS2 data was acquired in profile mode.

The raw output files of IsobarQuant (protein.txt – files) were processed using R. Only proteins quantified with at least two unique peptides were considered for the analysis. 183 proteins passed the quality control filters. Raw TMT intensities (signal_sum columns) were first cleaned for batch effects using limma[80] and further normalized using vsn (variance stabilization normalization.[81] Different normalization coefficients were estimated for DMSO and AEP conditions in order to maintain the abundance difference. Proteins were tested for differential expression using the limma package. The replicate information was added as a factor in the design matrix given as an argument to the 'lmFit' function of limma. A protein was annotated as a hit with a false discovery rate (fdr) smaller 5% and a fold-change of at least 100% and as a candidate with a fdr below 20% and a fold-change of at least 50%. All annotated protein identifiers were aligned with known *Hydra vulgaris* proteins (Local Alignment Search Tool (BLAST), NCBI). The hit proteins and candidate proteins were paired with the corresponding BLAST results (Table S1). An InterProScan analysis (EMBL-EBI) was performed on all protein domains to annotate them with a list of ECM identifiers published by Naba et al.[82]